

Magneto-electronic and optical properties of carbon nanotubes

F. L. Shyu,¹ C. P. Chang,² R. B. Chen,³ C. W. Chiu,⁴ and M. F. Lin⁴

¹*Department of Physics, Chinese Military Academy, Kaohsiung, Taiwan 830, The Republic of China*

²*Center for General Education, Tainan Woman's College of Art and Technology, Tainan, Taiwan 71002, The Republic of China*

³*Department of Electrical Engineering, Cheng Shiu Institute Technology, Kaohsiung, Taiwan 842, The Republic of China*

⁴*Department of Physics, National Cheng Kung University, Tainan, Taiwan 701, The Republic of China*

(Received 23 July 2002; published 17 January 2003)

Magneto-electronic and optical properties of carbon nanotubes are, respectively, studied within the sp^3 tight-binding model and the gradient approximation. They strongly depend on the magnitude and the direction of the magnetic field, the nanotube geometry (radius and chiral angle), and the Zeeman splitting. The magnetic field would lead to the change of energy gap, the destruction of state degeneracy, and the coupling of different angular momenta. Hence there are magnetic-field-dependent absorption frequencies and more absorption peaks. The types of carbon nanotubes predominate in the band structure and thus the range of absorption frequencies and the number of absorption peaks. The Zeeman splitting makes the semiconductor-metal transition occur at lower magnetic flux. It metalizes armchair carbon nanotubes in the presence of the perpendicular magnetic field. However, it does not affect the optical excitations except for metallic carbon nanotubes.

DOI: 10.1103/PhysRevB.67.045405

PACS number(s): 78.66.-w, 73.20.Mf

I. INTRODUCTION

Carbon nanotubes have prompted a lot of studies since their discovery by Iijima¹ in 1991, such as electronic structures²⁻¹⁶ and optical properties.¹⁷⁻²⁹ A single-wall carbon nanotube is a rolled-up graphite sheet,⁶ the structure of which is thus fully specified by a two-dimensional (2D) lattice vector $\mathbf{R}_x = m\mathbf{a}_1 + n\mathbf{a}_2$, where \mathbf{a}_1 and \mathbf{a}_2 are primitive lattice vectors of a graphite sheet. The radius and the chiral angle of a (m, n) carbon nanotube are, respectively, $R_d = |\mathbf{R}_x|/2\pi = b\sqrt{3(m^2 + mn + n^2)}/2\pi$ and $\theta = \tan^{-1}[-\sqrt{3}n/(2m+n)]$. $b = 1.42 \text{ \AA}$ is the C-C bond length. A carbon nanotube is a semiconductor or a metal, which depends on both radius and chirality.²⁻⁸ The electronic structure is strongly affected by the magnetic field.¹⁰⁻¹⁶ The optical excitations directly reflect its characteristics. In this work, the sp^3 tight-binding model with the curvature effects is utilized to calculate the magneto-electronic structure. Furthermore, the magneto-optical properties are studied by means of evaluating the optical-absorption function. The dependence on the nanotube geometry (R_d and θ), the direction and the magnitude of the magnetic field, and the Zeeman splitting are investigated.

There are three types of carbon nanotubes according to their energy gaps (E_g 's).^{5-6,8-9} A (m, n) carbon nanotube is (I) a gapless metal for $m=n$, (II) a narrow-gap semiconductor for $m \neq n$ and $2m+n=3I$ (I is an integer), and (III) a moderate-gap semiconductor for $2m+n \neq 3I$. Energy gaps are, respectively, inversely proportional to R_d^2 and R_d for type-II and type-III carbon nanotubes. From the sp^3 ($2p_z$)⁸ tight-binding model,⁹ energy gaps of type-II carbon nanotubes are given by the approximate relation $E_g \approx 5\gamma_0 b^2 \cos 3\theta/16R_d^2$ ($3\gamma_0 b^2 \cos 3\theta/16R_d^2$; $-\gamma_0$ is the nearest-neighbor resonance integral of $2p_z$ orbitals). This model includes the curvature effects, the misorientation of $p\pi$ orbitals, as well as the mixing of $p\pi$ and $sp^2\sigma$ orbitals. The predicted energy gaps are successful for understanding

the experimental measurements of the low-frequency optical-absorption spectra ($\omega < 0.1 \gamma_0$).²⁰ Each carbon nanotube has many 1D parabolic subbands except that the subbands nearest to the Fermi level ($E_F=0$) in an armchair (m, m) nanotube are linear. That is to say, all subbands have divergent density of states (DOS) in $1/\sqrt{E}$ form except the finite DOS of the linear subbands. The 1D van Hove singularities (vHs) in the DOS would play an important role on the optical-absorption spectra.

Electronic structures in the presence of the magnetic field are studied within the effective-mass approximation¹⁰ and the tight-binding model.¹¹⁻¹⁸ The magnetic field would affect energy dispersions and energy gaps. Furthermore, it leads to the oscillatory behavior. Electronic structures exhibit the periodical Aharonov-Bohm (AB) oscillations with a period $\phi_0 = hc/e$, if the magnetic field is parallel to the nanotube axis and the Zeeman splitting is neglected. The AB effect can be identified in the magnetophysical properties, e.g., magnetoresistance.¹⁷⁻¹⁸ Only $2p_z$ orbitals are taken into account in the above-mentioned studies. The sp^3 tight-binding model, with the curvature effects and the Zeeman splitting, can reveal more detailed electronic properties.

There have been some experimental studies on the optical excitation spectra.¹⁹⁻²⁵ These measurements show that the absorption spectra exhibit rich absorption peaks, owing to the 1D vHs. Such prominent peaks are determined by radius and chiral angle. For example, the first absorption peak, respectively, occurs at 10–20 meV (Ref. 22) and 0.5–0.7 eV (Refs. 20–21 and 23–25) for type-II and type-III carbon nanotubes with $R_d \sim 6-7 \text{ \AA}$. The theoretical studies are mainly focused on the π -electronic optical excitations.²⁶⁻³² They could explain the experimental results, such as the first absorption peak^{9,31-32} and the special absorption peak at $2\gamma_0$.³¹⁻³² The magneto-optical-absorption spectra are predicted to exhibit the periodical AB oscillations and depend on the direction of electric polarization and magnetic field.²⁶⁻²⁷

We use the sp^3 tight-binding model to calculate the mag-

netoenergy bands and the gradient approximation³³ to evaluate the magneto-optical-absorption function. Comparison with the previous studies^{10–16,26–27} is also made. Our study shows that electronic properties are very sensitive to changes in the magnitude and the direction of the magnetic field, the nanotube geometry (radius and chiral angle), and the Zeeman splitting. The magnetic field would induce the change of energy gap, the destruction of state degeneracy, and the coupling of different angular momenta. Such effects are directly reflected in the optical excitations. There are magnetic-field-dependent absorption frequencies and more absorption peaks. The low-energy electronic structures are mainly determined by the types of carbon nanotubes, and so do the range of absorption frequencies and the number of absorption peaks. The Zeeman splitting could reduce the energy gap and destroy the periodicity of the AB oscillations. It thoroughly metalizes armchair carbon nanotubes when the magnetic field is perpendicular to the nanotube axis. On the other hand, the Zeeman splitting hardly affects the optical excitations except for metallic carbon nanotubes.

This paper is organized as follows. The magnetoelectronic structures are calculated from the sp^3 tight-binding model. The magnetic-field-dependent energy gap is studied in Sec. II. The gradient approximation³³ is used to evaluate the optical-absorption function. The calculated magneto-optical spectra are discussed in Sec. III. Finally, Sec. IV contains the concluding remarks.

II. MAGNETOELECTRONIC PROPERTIES

We first see the sp^3 tight-binding model in the absence of the magnetic field. The number of carbon atoms in a primitive unit cell is $N_u = 4\sqrt{(m^2 + mn + n^2)(p^2 + pq + q^2)}/3$. (p, q) corresponds to the primitive vector perpendicular to the vector of (m, n) . As a result of the periodical boundary condition along the azimuthal direction, band structures without the magnetic field only involve two independent atoms, A and B . The calculations of band structure are similar to those done for a graphite sheet. The Hamiltonian is described by a 8×8 Hermitian matrix. According to A atom and B atom, it can be decomposed into four block matrices:

$$H_{A_i, A_j}(\mathbf{k}) = H_{B_i, B_j}(\mathbf{k}) = E_i \delta_{ij},$$

$$H_{A_i, B_j} = \sum_{l=1,2,3} h_{ij}^{(l)} \exp[i\mathbf{k} \cdot (\mathbf{r}_l - \mathbf{r}_A)],$$

$$H_{B_i, A_j} = \sum_{l'=1,2,3} h_{ij}^{(l')} \exp[i\mathbf{k} \cdot (\mathbf{r}_{l'} - \mathbf{r}_B)]. \quad (1)$$

Each block matrix is a 4×4 matrix. i represents the basis states of s and p orbitals. \mathbf{r}_A and \mathbf{r}_B are, respectively, positional vectors for the A atom and the B atom. The nearest-neighbor atom is at \mathbf{r}_l . The cylindrical coordinates (r, Φ, z) are convenient in taking into account the curvature effects. $\mathbf{r}_A = (R_d, 0, 0)$ and $\mathbf{r}_l = (R_d, \Phi_l, z_l)$. Φ_l 's and z_l 's for the three nearest-neighbor atoms are $\Phi_1 = -b \cos(\pi/6 - \theta)/R_d$, $\Phi_2 = b \cos(\pi/6 + \theta)/R_d$, $\Phi_3 = b \cos(\pi/2 - \theta)/R_d$, $z_1 = -b \sin(\pi/6 - \theta)$, $z_2 = -b \cos(\pi/3 - \theta)$, and $z_3 = b \cos(\theta)$,

respectively. Similar results are obtained for \mathbf{r}_B and $\mathbf{r}_{l'}$. The matrix elements $h_{ij}^{(l)}$'s in Eq. (1) are given by

$$h_{rr}^{(l)} = V_{pp\pi} \cos \Phi_l + 4(V_{pp\pi} - V_{pp\sigma}) \sin^4(\Phi_l/2) R_d^2/b^2,$$

$$h_{r\Phi}^{(l)} = V_{pp\pi} \sin \Phi_l - 4(V_{pp\pi} - V_{pp\sigma}) \sin^3(\Phi_l/2) \cos(\Phi_l/2) R_d^2/b^2,$$

$$h_{\Phi\Phi}^{(l)} = V_{pp\pi} \cos \Phi_l - (V_{pp\pi} - V_{pp\sigma}) \sin^2(\Phi_l) R_d^2/b^2,$$

$$h_{rz}^{(l)} = -2(V_{pp\pi} - V_{pp\sigma}) \sin^2(\Phi_l/2) R_d z_l/b^2,$$

$$h_{\Phi z}^{(l)} = -(V_{pp\pi} - V_{pp\sigma}) \sin(\Phi_l) R_d z_l/b^2,$$

$$h_{zz}^{(l)} = V_{pp\pi} - (V_{pp\pi} - V_{pp\sigma}) z_l^2/b^2,$$

$$h_{sr}^{(l)} = -2V_{sp\sigma} \sin^2(\Phi_l/2) R_d/b,$$

$$h_{s\Phi}^{(l)} = V_{sp\sigma} \sin(\Phi_l) R_d/b,$$

$$h_{sz}^{(l)} = V_{sp\sigma} z_l/b,$$

$$h_{ss}^{(l)} = V_{ss\sigma}. \quad (2)$$

$h_{z\Phi}^{(l)} = h_{\Phi z}^{(l)}$, $h_{\Phi r}^{(l)} = -h_{r\Phi}^{(l)}$, $h_{zr}^{(l)} = -h_{rz}^{(l)}$, $h_{rs}^{(l)} = h_{sr}^{(l)}$, $h_{\Phi s}^{(l)} = -h_{s\Phi}^{(l)}$; $h_{zs}^{(l)} = -h_{sz}^{(l)}$. The suffixes s, r, Φ , and z are, respectively, $s, p_\pi(p_z), p_{\sigma_1}$, and p_{σ_2} . $h_{rr}^{(l)}$ ($h_{r\Phi}^{(l)}$ and $h_{rz}^{(l)}$) is related to the misorientation of $p\pi$ orbitals (the mixing of $p\pi$ and $sp^2\sigma$ orbitals).⁹ The tight-binding parameters are as follows.⁷ The s orbital energy is $E_s = -7.3$ eV below the triply degenerate p orbitals taken as the zero of energy ($E_p = 0$). The Slater-Koster hopping parameters for the nearest-neighbor pairs are $V_{ss\sigma} = -4.30$ eV, $V_{sp\sigma} = 4.98$ eV, $V_{pp\sigma} = 6.38$ eV, and $V_{pp\pi} = -2.66$ eV ($= -\gamma_0$). Electronic states are characterized by the angular momentum J ($= k_x R_d = 1, 2, \dots, N_u/2$) and the longitudinal wave vector k_z ($-\pi \leq k_z R_d \leq \pi$). The discrete J 's come from the periodical boundary condition. $R_z = b\sqrt{3(p^2 + pq + q^2)}$ is the periodical distance along the nanotube axis.

When a carbon nanotube is threaded by a uniform magnetic field along the nanotube axis, the angular momentum changes from J into $J + \phi/\phi_0$. The magnetic flux is $\phi = \pi R_d^2 B$. The angular momentum keeps decoupled; that is, J is still a good quantum number. But on the other hand, the different J 's would couple one another as the magnetic field deviates from the nanotube axis. The angle between the magnetic field and the tube axis is assumed to be α , i.e., $\mathbf{B} = B \cos \alpha \hat{z} + B \sin \alpha \hat{\Phi} = B_{\parallel} \hat{z} + B_{\perp} \hat{\Phi}$. The parallel magnetic field (B_{\parallel}) induces the shift [$k_x \rightarrow k_x + \phi \cos(\alpha)/(\phi_0 R_d)$], and the perpendicular magnetic field (B_{\perp}) leads to the coupling of different J 's or k_x 's. For B_{\perp} , the total carbon atoms in a primitive cell are included in the band-structure calculations. The vector potential in the presence of B_{\perp} is chosen as

$$\mathbf{A} = R_d B_{\perp} \sin\left(\frac{x}{R_d}\right) \hat{z}, \quad (3)$$

where $x=R_d\Phi$. \mathbf{A} is independent of z , so the axial wave vector k_z remains a good quantum number. The dependence on x means that the different k_x 's or J 's are no longer decoupled.^{10–15} All the k_x 's need to be taken into account in the Hamiltonian matrix simultaneously. The vector potential will induce a phase factor $G_{\mathbf{R}}=\int_{\mathbf{R}^A}^{\mathbf{R}^B}\mathbf{A}(\mathbf{D})\cdot d\mathbf{D}$ in the tight-binding function. Now, each Hamiltonian block matrix in Eq. (1) changes from a 4×4 matrix into a $2N_u\times 2N_u$ matrix. The Hamiltonian matrix element between site A with k_x state and site B with k_x' state is given by

$$\langle\Phi_{k_x'}^{Bj}|H|\Phi_{k_x}^{Ai}\rangle=\frac{2h_{ij}}{N_u}\sum_{\mathbf{R}^A}\sum_{\mathbf{R}^B}e^{-i\Delta k_x x}e^{-i(k_x'+\phi\cos\alpha/\phi_0R_d)\Delta x}\times e^{-ik_z\Delta z}e^{i(e/\hbar)\Delta G},\quad(4)$$

where the phase difference due to B_{\perp} is

$$\Delta G=G_{\mathbf{R}^A}-G_{\mathbf{R}^B}=\frac{\phi\Delta z\sin\alpha}{\pi\Delta x}\left(\cos\frac{x}{R_d}-\cos\frac{x+\Delta x}{R_d}\right),$$

$$\Delta x\neq 0,$$

$$=\frac{\phi\Delta z\sin\alpha}{\pi R_d}\sin\frac{x}{R_d},\quad\Delta x=0.\quad(5)$$

$\mathbf{R}^A=(x,z)$, $\mathbf{R}^B=(x',z')$, and $\Delta\mathbf{R}=\mathbf{R}^B-\mathbf{R}^A=(\Delta x,\Delta z)$. The effect of B_{\parallel} is added in Eq. (4). The other three block matrices have the similar formula. The $4N_u\times 4N_u$ Hamiltonian matrix is thus constructed for any field direction.

By diagonalizing the Hamiltonian, we obtain energy dispersion $E^{c,v}(J,k_z,\phi)$ and wave function $\Psi^{c,v}(J,k_z,\phi)$. The superscripts v and c , respectively, represent the occupied valence bands and the unoccupied conduction bands. At $\alpha\neq 0^\circ$ ($\alpha=0^\circ$), the wave function is the linear combination of the $4N_u$ (8) tight-binding functions, and it is composed of the different J 's (the same J). Although there exists the coupling of angular momenta, the wave function is principally dominated by J at $\phi<\phi_0/3$. For simplicity, wave function and energy dispersion are denoted as a function of J . The magnetostate energy is the sum of the band energy plus the spin- B interaction energy, i.e., $E^{c,v}(J,k_z;\sigma,\phi)=E^{c,v}(J,k_z;\phi)+E(\sigma,\phi)$. $E(\sigma,\phi)=g\sigma\phi/m^*R_d^2\phi_0$. The g factor is taken to be the same as that (~ 2) of the pure graphite. $\sigma=\pm 1/2$ is the electron spin and m^* is the bare electron mass. The Zeeman splitting would lead to the rigid shift for the spin-up and spin-down states. It is neglected except that it has to be specially emphasized. For example, the Zeeman splitting affects the absorption spectra only when carbon nanotubes are gapless metals. The number of the total carriers is fixed during the variation of ϕ . The ϕ dependence of the Fermi level is examined to be very weak, i.e., $E_F(\phi)\approx 0$.

Three types of carbon nanotubes, the type-I (10, 10) nanotube, the type-II (18, 0) nanotube, and the type-III (17, 0) nanotube, are chosen for a model study. They have the nearly same radii. We first see the type-I (10, 10) nanotube. The low-energy magnetoband structures, without $E(\sigma,\phi)$, are shown in Fig. 1(a). There are linear bands intersecting at the

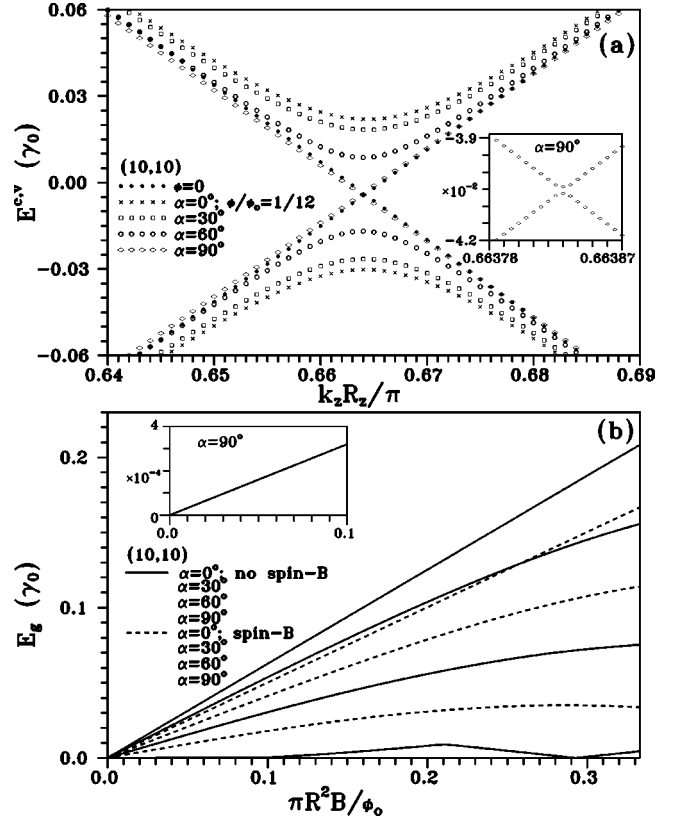


FIG. 1. (a) The energy bands nearest to the Fermi level are shown for the type-I (10, 10) nanotube at $\phi=\phi_0/12$ and different α 's, and $\phi=0$. (b) The magnetic-flux-dependent energy gaps are calculated at different α 's. The solid and dashed curves, respectively, correspond to those without and with the spin- B interactions. Also shown in the insets are the detailed results at $\alpha=90^\circ$. The several identical curves are plotted from $\alpha=0^\circ$ to $\alpha=90^\circ$.

Fermi level in the absence of magnetic flux. The (10, 10) nanotube is a gapless metal at $\phi=0$. The nondegenerate linear bands, which are described by $J=N_u/4=10$, exist at $k_z R_z\sim\pm 2\pi/3$. The magnetic flux would make the linear bands change into the parabolic bands. It causes an energy gap and a blue shift in the wave vector of the band-edge state. A similar shift could also be found in nonzigzag carbon nanotubes ($m\neq 0$). The magnetic flux affects the state degeneracy. Energy bands of J and $N_u/2-J$ are doubly degenerate except for those of $J=N_u/4$ and $J=N_u/2$. The effects of ϕ on J and $N_u/2-J$ are different, which thus leads to the destruction of the double degeneracy [Fig. 4(a)]. The above-mentioned effects due to the magnetic flux are relatively prominent, when the direction of the magnetic field approaches the nanotube axis. The magnetic flux at $\alpha\neq 0^\circ$ also induces the coupling of different J 's. Such coupling is strong only at large ϕ and α . It is weak for the type-I (10, 10) nanotube at $\phi=\phi_0/12$; therefore each energy band is approximately described by the decoupled angular momentum.

The variation of energy gap with magnetic flux deserves a closer investigation. Figure 1(b) presents the magnetic-flux-dependent energy gap for the type-I (10, 10) nanotube at $\phi\leq\phi_0/3$ and different α 's. E_g , without the Zeeman splitting, increases with ϕ monotonously except at large α . The oscil-

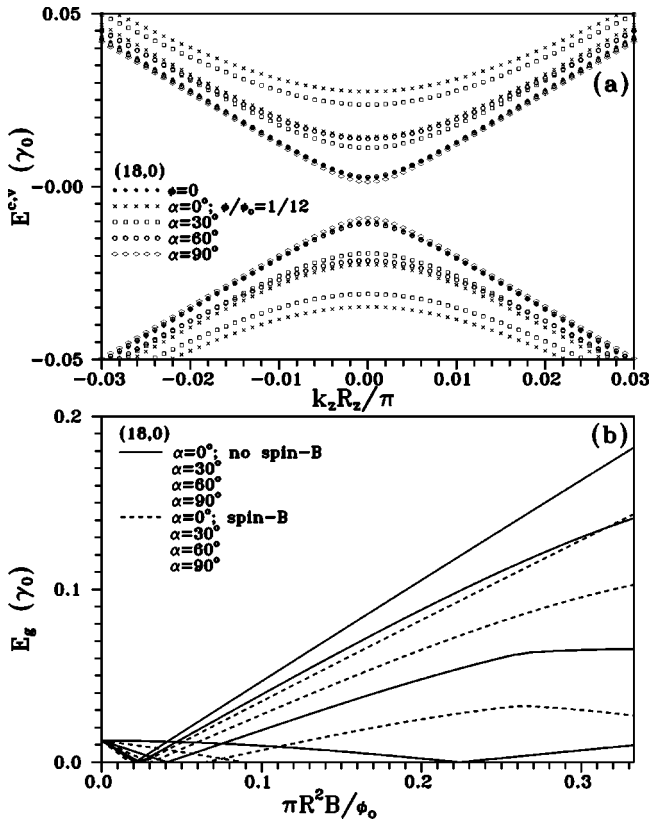


FIG. 2. Same plot as Fig. 1, but shown for the type-II (18, 0) nanotube. The several identical curves in (b) are plotted from $\alpha = 0^\circ$ to $\alpha = 90^\circ$.

latory behavior exists at large α , e.g., at $\alpha = 90^\circ$. It is associated with the oscillatory feature of the phase difference ΔG in the Hamiltonian matrix element [Eq. (4)].¹⁴ E_g decreases in the increasing of α . This result means that energy gap is comparatively easily modulated by the parallel magnetic field. E_g changes from zero into a finite value at vanishing magnetic flux; that is, the metal-semiconductor transition (MST) happens at $\phi_{\text{MST}} = 0$. Such transition occurs more frequently at large α . The spin- B interaction causes the splitting of the spin-up and spin-down states and thus reduces energy gap. It metalizes the (10, 10) nanotube at any magnetic flux for sufficiently large α ($> 81^\circ$), since the double spin- B interaction energy [$2\phi/m^*R_d^2\phi_0$] is in excess of energy gap due to the magnetic field. All type-I armchair nanotubes exhibit the metalization behavior in the presence of the perpendicular magnetic field, mainly owing to the Zeeman splitting. The metallic carbon nanotubes have free carriers, so they are expected to own the low-frequency collective excitations.³⁵ This problem is under current investigation.

At $\phi = 0$, the type-II (18, 0) nanotube has parabolic energy dispersions near the Fermi level and a small energy gap, as shown in Fig. 2(a). The curvature effects are the main cause.⁹ The two parabolic bands correspond to $J = 12$ and $J = 24$. The double degeneracy is clearly destroyed by the magnetic flux. However, the band-edge state keeps at $k_z = 0$ during the variation of ϕ . The energy gap, as shown in Fig. 2(b), decreases as ϕ gradually grows. E_g without the spin- B interaction vanishes at small ϕ_{MST} , where energy disper-

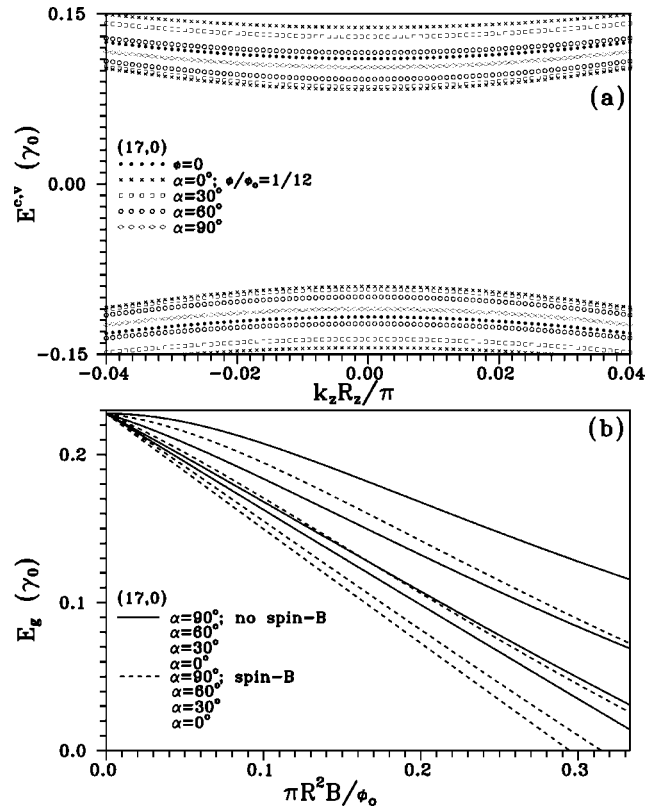


FIG. 3. Same plot as Fig. 1, but shown for the type-III (17, 0) nanotube. The several identical curves in (b) are plotted from $\alpha = 90^\circ$ to $\alpha = 0^\circ$.

sions are linear. The main effects of the Zeeman splitting are to reduce ϕ_{MST} and metalize the type-II nanotubes at sufficiently large α and ϕ . There are three important differences between type-I carbon nanotubes and type-II carbon nanotubes (or type-III carbon nanotubes). They include the destruction of the double degeneracy for the energy bands nearest to the Fermi level, the dependence of the band-edge state on ϕ , and the zero or nonzero ϕ_{MST} .

The magnetoband structures of the type-III (17, 0) nanotube are shown in Fig. 3(a). It has a large energy gap in the absence of ϕ . The magnetic flux leads to the splitting of the doubly degenerate energy bands, but not the shift of the $k_z = 0$ band edge. It could effectively reduce the energy gap, as shown in Fig. 3(b). E_g decreases with ϕ monotonously even at large α . The oscillatory ϕ dependence, as seen in type-I and type-II carbon nanotubes at large α [Figs. 1(b) and 2(b)], is not present. The MST of the type-III carbon nanotubes happens at $\phi_{\text{MST}} \sim \phi_0/3$. However, for all carbon nanotubes, the variation of E_g with ϕ is relatively quick at small α . The above-mentioned magnetoenergy gap can be directly verified by scanning tunneling spectroscopy,^{36–38} transport measurements,³⁹ and optical-absorption spectroscopy.^{19–25}

Our study is compared with the previous studies. From the sp^3 tight-binding model, the ϕ dependence of the energy gap is different for type-I, type-II, and type-III carbon nanotubes [Figs. 1(b), 2(b), and 3(b)]. Energy gaps of type-I carbon nanotubes grow in the slow increasing of ϕ , while the opposite is true for type-II carbon nanotubes. Such difference

mainly comes from the curvature effects.⁹ It cannot be found in the $2p_z$ tight-binding calculations.^{16,13} An energy gap at $\phi \rightarrow 0$ would determine whether carbon nanotubes are paramagnetic or diamagnetic.^{11,12} The curvature effects might dominate over magnetic properties of type-II carbon nanotubes. A simple relation between the nanotube radius and the ϕ -dependent energy gap is examined. The previous study by Lu¹⁶ shows that $E_g(\phi)$ is inversely proportional to R_d for any field direction. However, there is no simple relation in another study by Ajiki and Ando.¹³ This work is consistent with the latter. For the perpendicular magnetic field, the Zeeman splitting can thoroughly metalize type-I carbon nanotubes. It is very important in clarifying the low-energy physical properties, such as magnetoplasmons and magnetization.

The metalization behavior is absent in the previous studies. The spin- B interaction energy increases with magnetic field linearly. The Zeeman splitting apparently destroys the periodical AB oscillations in electronic^{10,16} and optical properties.^{26–27}

III. MAGNETO-OPTICAL SPECTRA

The above-mentioned features of the magnetoband structures will be directly reflected in the optical excitations. At $T=0$, electrons are excited from the occupied valence bands to the unoccupied conduction bands. The magneto-optical-absorption function of the (m, n) carbon nanotube is given by³⁴

$$A(\omega; \phi) \propto \sum_{J, J'} \int_{1\text{stBZ}} \frac{dk_z}{2\pi} \cdot \frac{\left| \langle \Psi^c(J', k_z; \sigma \phi) | \frac{\hat{\mathbf{E}} \cdot \mathbf{P}}{m_e} | \Psi^v(J, k_z; \phi) \rangle \right|^2}{\omega_{vc}^2(J, J', k_z; \phi)} \cdot \left(\frac{\Gamma}{[\omega - \omega_{vc}(J, J', k_z; \phi)]^2 + \Gamma^2} - \frac{\Gamma}{[\omega + \omega_{vc}(J, J', k_z; \phi)]^2 + \Gamma^2} \right). \quad (6)$$

$\omega_{vc}(J, J', k_z; \phi) = E^c(J', k_z; \phi) - E^v(J, k_z; \phi)$ is the interband excitation energy. $\Gamma (= 0.001\gamma_0)$ is the energy width from various deexcitation mechanisms. The square of the velocity matrix element in Eq. (6) is evaluated within the gradient approximation.³³ The electric polarization is assumed to be parallel to the nanotube axis. There exist two selection rules for the optical excitations that greatly simplify the calculations.^{26–32} One is that $\Delta k_z = 0$ in Eq. (6), which follows from the fact that for photons in the long-wavelength limit the initial- and final-state wave vectors are the same. Another is that the angular momentum is conserved during the vertical transitions. The wave function has $4N_u$ components made up of different J 's. Eight components, which correspond to a definite J , are treated as an entity. $\Delta J = 0$ means that the optical excitations from Ψ^v to Ψ^c for the components with the same J are allowed.

The Zeeman splitting is included in the calculations. It does not affect the low-frequency absorption spectra, when carbon nanotubes are semiconducting. That only the optical excitations from the same spin states are effective is responsible for this result. However, the Zeeman splitting in metallic carbon nanotubes can alter electron distribution and thus optical excitations. In short, the Zeeman splitting has to be taken into account in determining whether carbon nanotubes are semiconducting or metallic. For semiconducting carbon nanotubes, the optical excitation spectra, with and without the Zeeman splitting, are identical to each other.

DOS, which is associated with the number of excitation channels, is useful in explaining the optical-absorption spectra. It is defined as

$$D(\omega; \phi) = 2 \sum_{J, h=c, v} \int_{1\text{stBZ}} \frac{dk_z}{2\pi} \frac{\Gamma}{[\omega - E^h(J, k_z; \phi)]^2 + \Gamma^2}. \quad (7)$$

DOS of the type-I (10, 10) nanotube, without the Zeeman splitting, is shown in Fig. 4(a) at $\alpha = 0^\circ$ and various ϕ 's. At $\phi = 0$, the low-energy pleatou is due to the linear bands. The asymmetric peaks (vHs) at higher energy come from the doubly degenerate parabolic bands. The magnetic flux changes the linear energy dispersions and destroys the double degeneracy. Hence there are two new peaks at low energy and double peaks at others. The energy spacing (ω_s) between the two neighboring peaks is widened as ϕ increases. DOS of the low-energy peaks is enhanced by ϕ , since the parabolic bands nearest to the Fermi level become comparatively flat (or have smaller curvatures). The peaks at negative energy are approximately symmetric to those at positive energy, about the Fermi level. Furthermore, the symmetric two peaks have the same J . Also notice that the symmetry of band structure is somewhat destroyed by the mixing of the $p\pi$ and $sp^2\sigma$ orbitals. Tunneling spectroscopy measurements can be used to check the asymmetric peaks in DOS.³⁸

The vanishing velocity matrix prevents the optical excitations from the occupied linear band to the unoccupied linear band.^{26,31} The threshold interband excitations of the type-I (10, 10) nanotube do not exist at $\phi = 0$, as shown in Fig. 4(b). The second absorption peak, which occurs at $\omega_2 \sim 0.62\gamma_0$, results from the second energy bands close to the Fermi level [Fig. 4(a)]. Each energy band is described by a single angular momentum in the presence of ϕ and $\alpha = 0^\circ$. The optical

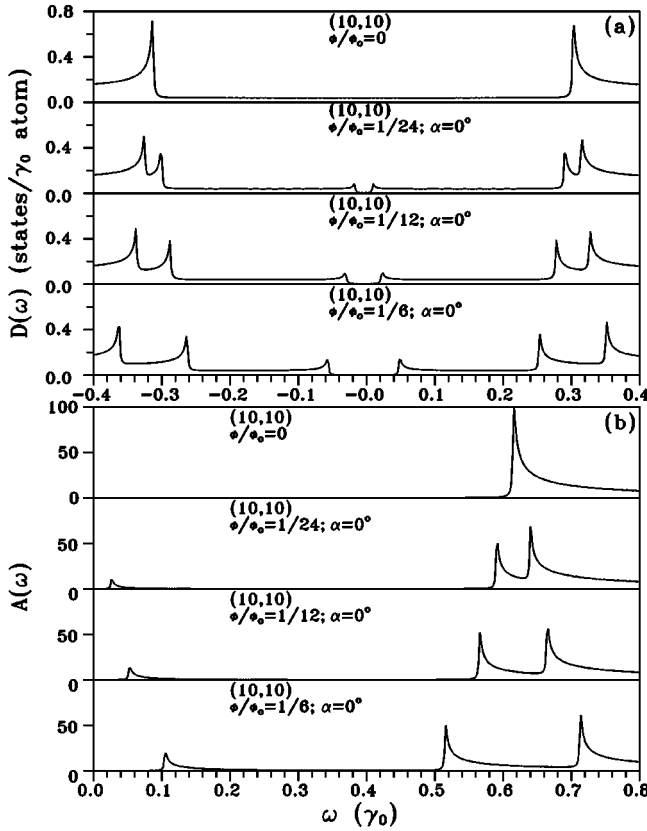


FIG. 4. (a) Density of states of the type-I (10, 10) nanotube at $\alpha=0^\circ$ and different ϕ 's. The corresponding absorption spectra are shown in (b).

excitations between the band-edge states of the two parabolic bands with the same J produce the asymmetric absorption peaks. These peaks are divergent in the square-root form at $\Gamma \rightarrow 0$, mainly owing to the vHs in the conduction and valence bands. For the first absorption peak, its frequency (ω_1) is energy gap without the spin- B interaction, but not that with the spin- B interaction [Fig. 1(b)]. Both frequency and intensity increase as ϕ grows. The enhancement of intensity is caused by the less dispersive parabolic bands. The magnetic flux also leads to double absorption peaks at higher frequency.

The nanotube geometry affects band structures and thus absorption peaks. Figure 5(a) shows DOS for different carbon nanotubes at $\phi = \phi_0/12$ and $\alpha = 0^\circ$. The type-I (10, 10) nanotube, the type-II (13, 7) nanotube, and the type-II (18, 0) nanotube have the different chiral angles. Their DOS's exhibit asymmetric peaks at $|\omega| < 0.05\gamma_0$ and $0.25\gamma_0 < |\omega| < 0.35\gamma_0$. That is to say, the energy range of peaks is the same for type-I and type-II carbon nanotubes. On the other hand, the differences in DOS's are mainly determined by armchair or nonarmchair structures ($\theta = -30^\circ$ or others). Armchair nanotubes have half the peaks compared with nonarmchair nanotubes. This result could be understood from the simple zone folding model.³¹ Moreover, the DOS is higher for the former. Armchair nanotubes thus exhibit fewer but stronger absorption peaks [Fig. 5(b)]. The number of interband excitation channels is proportional to the nanotube radius or the number of 1D subbands, as shown in Fig. 5(a)

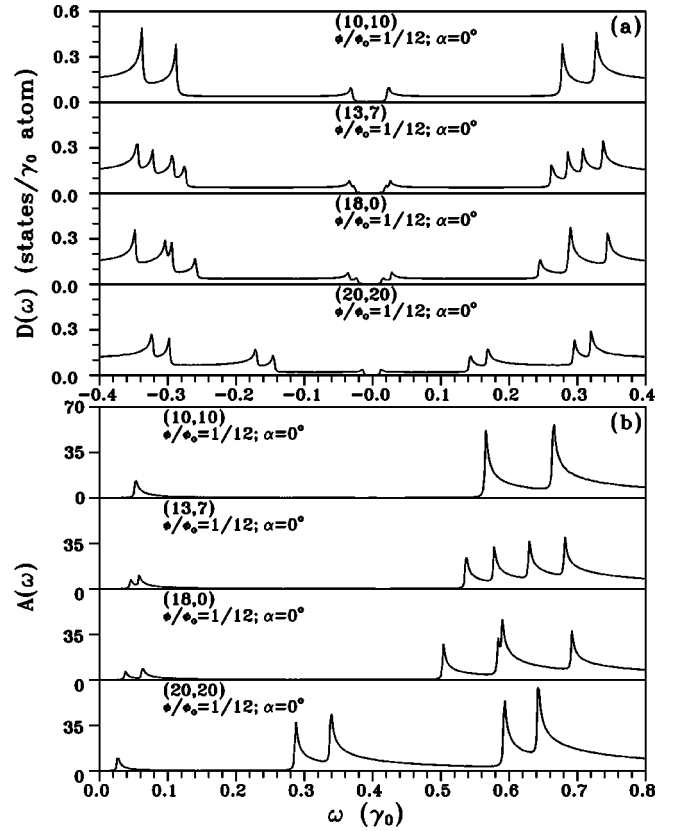


FIG. 5. Same plot as Fig. 4, but shown for type-I and type-II carbon nanotubes at $\phi = \phi_0/12$ and $\alpha = 0^\circ$.

for the type-I (20, 20) and (10, 10) nanotubes. The large nanotubes have more absorption peaks and lower threshold frequency [Fig. 5(b)]. As for the energy spacing between the two neighboring peaks, ω_s decreases in the increasing of radius or chiral angle.

The direction of the magnetic field plays an important role on electronic and optical properties. DOS of the type-I (10, 10) nanotube is shown in Fig. 6(a) at $\phi = \phi_0/12$ and different α 's. The main effect of B_{\parallel} is to induce the subband splitting except for the two energy bands near E_F . The larger B_{\parallel} is (the smaller α is), the wider the energy spacing between the two neighboring peaks is. The coupling of different J 's due to B_{\perp} is negligible at $\phi = \phi_0/12$. Only the optical excitations from the symmetric energy bands produce the strong absorption peaks, as shown in Fig. 6(b). To get the additional absorption peaks, the magnetic flux needs to be sufficiently high, e.g., $\phi = \phi_0/3$. At $\alpha = 90^\circ$, the perpendicular magnetic field hardly affects the state degeneracy. There are fewer absorption peaks. It is very special that the first absorption peak is absent. The main reasons are as follows. The energy bands nearest to the Fermi level are linear except at the neighborhood of band edges [Fig. 6(a)]. The Zeeman splitting makes the (10, 10) nanotube metallic, so there are no allowable optical excitations from the band-edge states with the different spin states. Moreover, the linear energy dispersions, as discussed earlier, have no contributions to absorption spectra. In addition, the type-II (18, 0) nanotube exhibits the similar

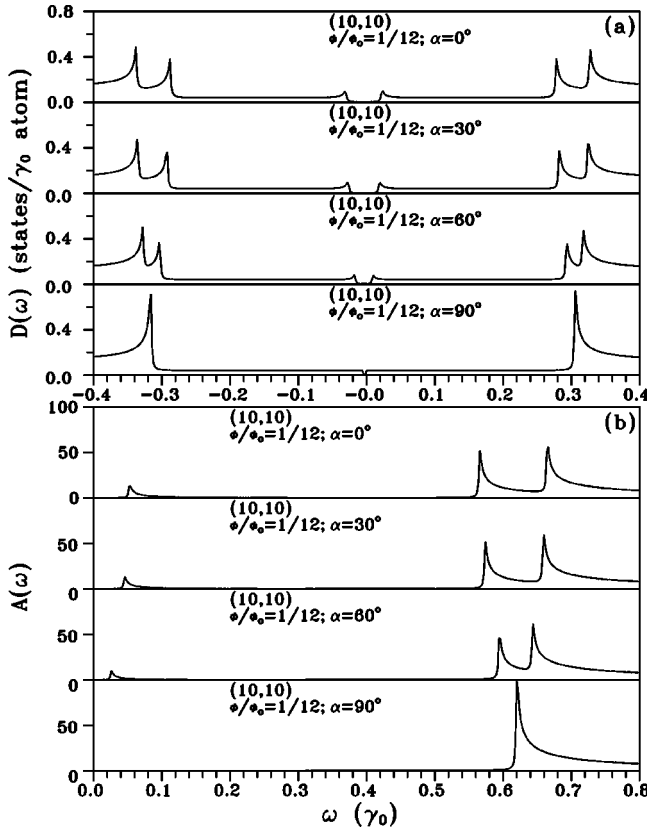


FIG. 6. Same plot as Fig. 4, but shown at $\phi = \phi_0/12$ and different α 's.

DOS and $A(\omega)$ except that the first absorption peak is present at $\alpha = 90^\circ$ and $\phi = \phi_0/12$ [Fig. 8(b)].

DOS of the type-III (17, 0) nanotube exhibits eight peaks at $0.08\gamma_0 < |\omega| < 0.22\gamma_0$, as shown in Fig. 7(a). As a result, at $\phi = 0^\circ$, the symmetric conduction and valence bands yield four absorption peaks at $0.16\gamma_0 < \omega < 0.44\gamma_0$ [Fig. 7(b)]. When the magnetic field deviates from the nanotube axis, each energy band is made up of different angular momenta (J and $J \pm 1$). The optical excitations from the asymmetric energy bands are allowed; therefore the coupling of different J 's causes two new absorption peaks at $\omega \sim 0.3\gamma_0$. Such peaks become stronger as α increases; that is, the coupling effect is more important at large α . They hardly exist in the type-I (10, 10) nanotube or the type-II (18, 0) nanotube [Fig. 6(b)]. It is relatively easy to see the coupling of different J 's in the type-III carbon nanotubes.

The α -dependent absorption frequencies are important in understanding the characteristics of absorption peaks. The frequencies (ω_i 's) of absorption peaks are shown in Fig. 8 for the type-I (10, 10) nanotube at $\phi = \phi_0/12$. The frequency of the first peak is $\omega_1 \sim 0.05\gamma_0$ at $\alpha = 0^\circ$. ω_1 is equal to the energy gap in the absence of the Zeeman splitting, and it decreases with α . The first peak is absent at sufficiently large α ($> 81^\circ$), where the (10, 10) nanotube is a gapless metal. The two neighboring peaks, the second peak and the third peak, have the largest energy spacing at $\alpha = 0^\circ$. Their frequencies are, respectively, $\omega_2 \sim 0.57\gamma_0$ and $\omega_3 \sim 0.67\gamma_0$. They gradually merge together in the increasing of α , since

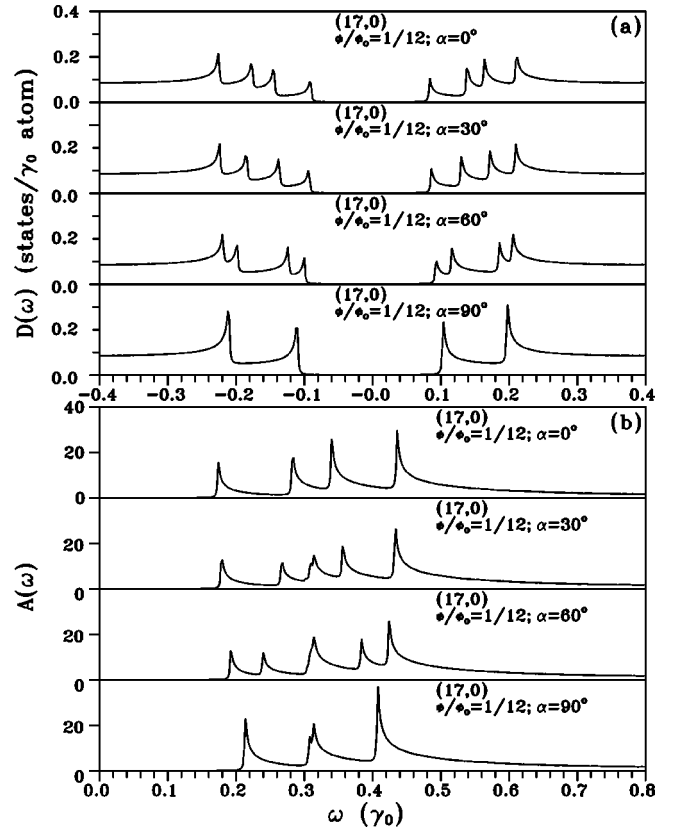


FIG. 7. Same plot as Fig. 4, but shown for the type-III (17, 0) nanotube at $\phi = \phi_0/12$ and different α 's.

the double degeneracy would be restored. The type-II (18, 0) nanotube is similar to the type-I (10, 10) nanotube, such as the frequency range of absorption peaks ($0.5\gamma_0 < \omega_i < 0.7\gamma_0$) and the merger of a pair of peaks at $\alpha = 90^\circ$. However, the number of absorption peaks is double for the former [Fig. 8(b)]. The absorption peaks of the type-III (17, 0) nanotube occur at the different frequency range [$0.16\gamma_0 < \omega_i < 0.44\gamma_0$ in Fig. 8(c)]. The two additional peaks with $\omega_i \sim 0.3\gamma_0$ could survive at sufficiently large α , when the coupling of different angular momenta is strong. The difference in absorption frequency range is useful in distinguishing type-III carbon nanotubes from type-I or type-II carbon nanotubes. The Zeeman splitting does not affect the number of absorption peaks and absorption frequencies except the disappearance of the first peak from type-I and type-II carbon nanotubes. The experimental measurements on the magnetoabsorption spectra can verify the predicted absorption frequencies.

The effective-mass approximation had been used to study magnetoelectronic and optical spectra.²⁶⁻²⁷ There are some similar results. The optical spectra strongly depend on the direction and the magnitude of the magnetic field. Moreover, all the absorption peaks can exist in the parallel electric polarization. However, such works do not involve the Zeeman splitting and the curvature effects. The present work can provide more detailed optical properties, e.g., the absorption frequencies and the number of absorption peaks.

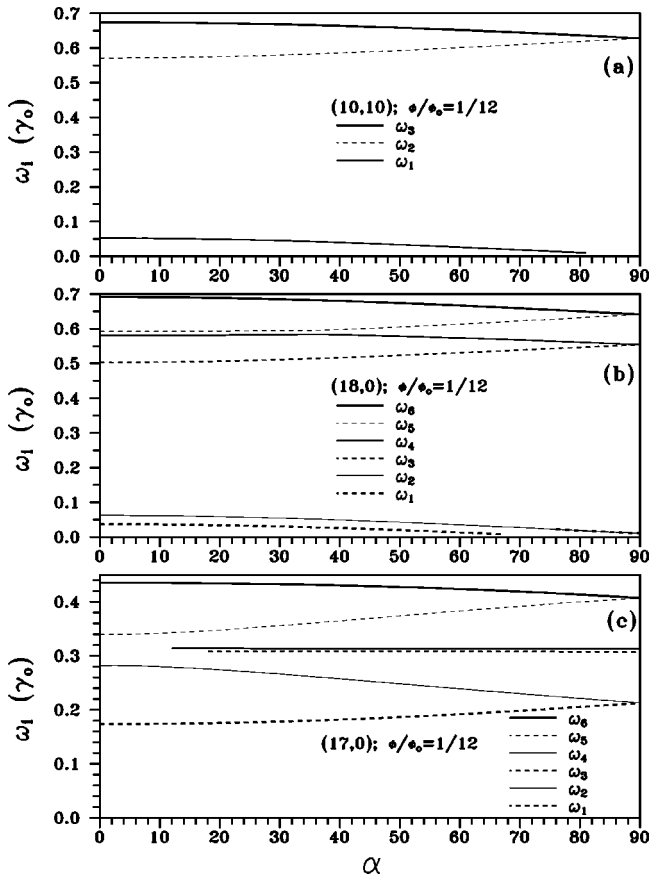


FIG. 8. The α -dependent absorption frequencies are calculated for (a) the type-I (10, 10) nanotube, (b) the type-II (18, 0) nanotube, and (c) the type-III (17, 0) nanotube.

IV. CONCLUDING REMARKS

In this work, we have studied the magnetoelectronic and optical properties of single-walled carbon nanotubes. They

are significantly affected by the nanotube geometry (radius and chiral angle), the magnitude and the direction of the magnetic field, and the Zeeman splitting. The predicted physical properties, energy gap, density of states, and absorption spectrum can be tested by scanning tunneling spectroscopy,^{36–38} transport measurements,³⁹ and optical-absorption spectroscopy.^{19–25} The curvature effects and the Zeeman splitting are included in the calculations. There exist certain important differences between the present study and the previous studies,^{10,13,16} such as the ϕ dependence of energy gap for type-II carbon nanotubes, the relation between energy gap and magnetic field, and the metalization of type-I carbon nanotubes in the perpendicular magnetic field.

The nanotube geometry dominates the electronic properties, energy gap, state degeneracy, and number of energy bands. The differences among type-I, type-II, and type-III carbon nanotubes are directly reflected in the optical excitations, e.g., the number of absorption peaks and the range of absorption frequencies. The magnetic field results in the change of energy gap, the destruction of state degeneracy, and the coupling of different angular momenta. Hence there are magnetic-field-dependent absorption frequencies and more absorption peaks. The Zeeman splitting can effectively reduce energy gap, so it makes the semiconductor-metal transition display at lower magnetic flux. It can completely metalize type-I carbon nanotubes in the presence of the perpendicular magnetic field. The Zeeman splitting is expected to play an important role on the low-energy physical properties, e.g., magnetoplasmons³⁵ and magnetic susceptibility.^{11–12,16} However, it has no effect on the optical excitations except for metallic carbon nanotubes.

ACKNOWLEDGMENT

This work was supported in part by the National Science Council of Taiwan, the Republic of China, under Grant Nos. NSC 90-2112-M-006-007 and NSC 90-2112-M-145-003.

- ¹S. Iijima, *Nature (London)* **354**, 56 (1991).
- ²J. W. Mintmire, B. I. Dunlap, and C. T. White, *Phys. Rev. Lett.* **68**, 631 (1992).
- ³J. W. Mintmire and C. T. White, *Phys. Rev. Lett.* **81**, 2506 (1998).
- ⁴C. T. White and T. N. Todorov, *Nature (London)* **393**, 240 (1998).
- ⁵N. Hamada, S. I. Sawada, and A. Oshiyama, *Phys. Rev. Lett.* **68**, 1579 (1992).
- ⁶For the details of geometric structures see R. Saito, M. Fujita, G. Dresselhaus, and M. S. Dresselhaus, *Appl. Phys. Lett.* **60**, 2204 (1992); *Phys. Rev. B* **46**, 1804 (1992).
- ⁷J.-C. Charlier and Ph. Lambin, *Phys. Rev. B* **57**, 15 037 (1998).
- ⁸C. L. Kane and E. J. Mele, *Phys. Rev. Lett.* **78**, 1932 (1997).
- ⁹F. L. Shyu and M. F. Lin, *J. Phys. Soc. Jpn.* **71**, 1820 (2002).
- ¹⁰H. Ajiki and T. Ando, *J. Phys. Soc. Jpn.* **62**, 1255 (1993).
- ¹¹H. Ajiki and T. Ando, *J. Phys. Soc. Jpn.* **62**, 2470 (1993).
- ¹²H. Ajiki and T. Ando, *J. Phys. Soc. Jpn.* **64**, 4382 (1995).
- ¹³H. Ajiki and T. Ando, *J. Phys. Soc. Jpn.* **65**, 505 (1996).
- ¹⁴R. Saito, G. Dresselhaus, and M. S. Dresselhaus, *Phys. Rev. B* **50**, 14 698 (1994); **53**, 10 408(E) (1996).
- ¹⁵S. Roche, G. Dresselhaus, M. S. Dresselhaus, and R. Saito, *Phys. Rev. B* **62**, 16 092 (2000).
- ¹⁶J. P. Lu, *Phys. Rev. Lett.* **74**, 1123 (1995).
- ¹⁷A. Fujiwara, K. Tomiyama, H. Suematsu, M. Yumura, and K. Uchida, *Phys. Rev. B* **60**, 13 492 (1999).
- ¹⁸S. Roche and R. Saito, *Phys. Rev. Lett.* **87**, 246803 (2001).
- ¹⁹A. Thess, R. Lee, P. Nikolaev, H. Dai, P. Petit, J. Robert, C. Xu, Y. H. Lee, S. G. Kim, A. G. Rinzler, D. T. Colbert, G. E. Scuseria, D. Tamonek, J. E. Fischer, and R. E. Smalley, *Science* **273**, 483 (1996).
- ²⁰H. Kataura, Y. Kumazawa, Y. Maniwa, I. Umezumi, S. Suzuki, Y. Ohtsuka, and Y. Achiba, *Synth. Met.* **103**, 2555 (1999).
- ²¹O. Jost, A. A. Gorbunov, W. Pompe, T. Pichler, R. Friedlein, M. Knupfer, M. Reibold, H.-D. Bauer, L. Dunsch, M. S. Golden, and J. Fink, *Appl. Phys. Lett.* **75**, 2217 (1999).
- ²²A. Ugawa, A. G. Rinzler, and D. B. Tanner, *Phys. Rev. B* **60**, 11 305 (1999).
- ²³M. Ichida, S. Mizuno, Y. Tani, Y. Saito, and A. Nakamura, *J. Phys. Soc. Jpn.* **68**, 3131 (1999).

- ²⁴S. Kazaoui, N. Minami, H. Yamawaki, K. Aoki, H. Kataura, and Y. Achiba, *Phys. Rev. B* **62**, 1643 (2000).
- ²⁵J. Hwang, H. H. Gommans, A. Ugawa, H. Tashiro, R. Haggenmueller, K. I. Winey, J. E. Fischer, D. B. Tanner, and A. G. Rinzler, *Phys. Rev. B* **62**, 13 310 (2000).
- ²⁶H. Ajiki and T. Ando, *Physica B* **201**, 349 (1994).
- ²⁷H. Ajiki, *Phys. Rev. B* **65**, 233409 (2002).
- ²⁸T. Ando, *J. Phys. Soc. Jpn.* **66**, 1066 (1997).
- ²⁹M. F. Lin and K. W.-K. Shung, *Phys. Rev. B* **50**, 17 744 (1994).
- ³⁰M. F. Lin, F. L. Shyu, and R. B. Chen, *Phys. Rev. B* **61**, 14 114 (2000).
- ³¹M. F. Lin, *Phys. Rev. B* **62**, 13 153 (2000).
- ³²S. Tasaki, K. Maekawa, and T. Yamabe, *Phys. Rev. B* **57**, 9301 (1998).
- ³³L. G. Johnson and G. Dresselhaus, *Phys. Rev. B* **7**, 2275 (1973).
- ³⁴G. D. Mahan, *Many-Particle Physics* (Plenum, New York, 1990).
- ³⁵M. F. Lin and K. W.-K. Shung, *Phys. Rev. B* **48**, 5567 (1993).
- ³⁶J. W. G. Wildoer, L. C. Venema, A. G. Rinzler, R. E. Richard, and C. Dekker, *Nature (London)* **391**, 59 (1998).
- ³⁷T. W. Odom, J. L. Huang, P. Kim, and C. M. Lieber, *Nature (London)* **391**, 62 (1998).
- ³⁸P. Kim, T. W. Odom, J. L. Huang, and C. M. Lieber, *Phys. Rev. Lett.* **82**, 1225 (1999).
- ³⁹C. Zhou, J. Kong, and H. Dai, *Phys. Rev. Lett.* **84**, 5604 (2000).